*2019 Rock Dynamics Summit– Aydan et al. (eds)*
*© 2019 Taylor & Francis Group, London, ISBN 978-0-367-34783-3*

# Comparison of stress field change around a fault by dynamic fault rupture simulation using 3D-FEM

N. Iwata & R. Kiyota
*Chuden Engineering Consultants Co., Ltd., Hiroshima, Japan*

Ö. Aydan
*Department of Civil Engineering, University of the Ryukyus, Okinawa, Japan*

T. Ito
*Institute of Fluid Science, Tohoku University, Sendai, Japan*

F. Miura
*Graduate School of Science and Engineering, Yamaguchi University, Yamaguchi, Japan*

ABSTRACT: When we are able to evaluate earthquake-induced stress changes of the ground around ruptured faults and adjacent faults, it will be possible to improve the prediction accuracy of the magnitude and probability of future earthquakes. Generally, the interaction between active faults is represented by static Coulomb stress changes (ΔCFF) induced by fault rupturing. In most cases, ΔCFF is calculated based on the elasticity theory of dislocation; there are few studies where it is calculated by 3D-FEM. In this study, we conducted fault rupture simulations using 3D-FEM for simple models with a planar fault plane and homogeneous bedrock and examined the influence of fault type and initial stress distribution. As a result, ΔCFF calculated by 3D-FEM became considerably larger than that calculated by the elasticity theory of dislocation. Moreover, even when a fault type and seismic magnitude were the same, the distribution domain and quantity of ΔCFF differed greatly owing to the combination of analytical parameters.

## 1 INTRODUCTION

When we are able to estimate earthquake-induced stress changes of ground around ruptured faults and adjacent faults, it will be possible to evaluate rupture propagation and improve the prediction accuracy of the magnitude and probability of future earthquakes. Generally, the change of stress before and after an earthquake is evaluated by static Coulomb stress change (ΔCFF) (Stein et al. 1997, Toda et al. 1998, Hashimoto 1996). ΔCFF has been applied to earthquake-forecasting indexes that have been used to assess potential hazards related to earthquake activity. Seismic activities are enhanced by slight ΔCFF increases of 0.1 MPa (Toda et al. 1998). Examination by dynamic ΔCFF, i.e. Coulomb stress change during an earthquake, has been carried out recently, and there is a report that dynamic ΔCFF distribution matches aftershock activities than static ΔCFF distribution well (Kilb et al. 2002, Gomberg et al. 2003). However, in those studies, ΔCFF was calculated from static or dynamic stress changes using the assumed dislocation on the fault plane; the dynamic destruction process was not taken into account.

The present authors have examined a series of fault rupture simulations to estimate displacement and strong motions in the ground surface at the same time using the three-dimensional finite element method (3D-FEM) to consider the dynamic destruction process of the fault plane. This analytical method and modelling was proposed by Toki & Sawada (1988) and Mizumoto et al. (2005). The fault plane is assumed as bedrock discontinuities and is modelled by joint elements, and shear failure occurring at hypocentre spreads to surrounding areas with increasing shear stress. Iwata et al. (2018, 2019) conducted a fault rupture simulation for the 2014 Northern Nagano Earthquake induced by the Kamishiro Fault ($M_w$6.3) and found that the quantity and distribution shape of dislocation on the fault plane depended on the initial stress distribution and stiffness of the joint elements. Furthermore, the distribution shape of dislocation calculated by 3D-FEM was markedly different from the rectangle that was used for the strong motion prediction based on 'Recipe' by Irikura (2006).

In this study, we calculated static ΔCFF for simple fault rupture models using two methods: (i) elasticity theory of dislocation (Okada 1992) in a homogeneous half-space and (ii) fault rupture simulation by 3D-FEM. We then compared the influence of analytical method and fault type. Dynamic ΔCFF is also important for evaluating the influence on neighbouring faults; however, this was not considered in the present study.

## 2 OUTLINE OF ANALYTICAL METHOD

### 2.1 *Elasticity theory of dislocation*

In the elasticity theory of dislocation, stress and deformation are calculated mathematically in an elastic half-space with uniform isotropic elastic properties (following Okada (1992)). The fault sliding is given uniformly in rectangular sources. The difference in fault types is expressed by changing the input sliding direction. We used software Coulomb 3.3 (Toda et al. 2011).

### 2.2 *Fault rupture simulation by 3D-FEM*

If the equation of motion involves the rupture movement of the fault plane, it is necessary to treat the motion as a nonlinear problem. Therefore, it is appropriate to obtain a solution for the equation of motion not in the frequency domain but in the time domain. The destruction process of dislocation and the dynamic behaviour of ground are calculated by solving the equation of motion using the stress drop of dislocation as an external force. The equation of motion at time step $n$ is written as;

$$[M]\{\ddot{u}\}_n + [C]\{\dot{u}\}_n + [K]\{u\}_n = \{F(n,s)\} \tag{1}$$

where $[M]$ is mass matrix, $[C]$ is damping matrix, $[K]$ is stiffness matrix, $\{\ddot{u}\}$ is acceleration vector, $\{\dot{u}\}$ is velocity, $\{u\}$ is displacement and $\{F(n,s)\}$ is the external force vector calculated from the dynamic stress drop, where $n$ and respectively, stand for the time step and nodal pairs where fault rupture takes place. The damping matrix $[C]$ is obtained from the linear combination of $[M]$ and $[K]$, which is termed Rayleigh damping. Equation (1) is solved using the Newmark's $\beta$ method, $\beta = 0.25$, $\gamma = 0.5$, at each time interval. To solve the nonlinear equation of motion, we employed the load transfer method utilising the initial stiffness method (Toki & Sawada 1988, Tsuboi & Miura 1996).

The fault plane is modelled by joint elements, as shown in Figure 1. The shear spring $K_s$, $K_r$ and normal spring $K_n$ are connected between nodal points of solid elements and a sliding occurs according to the Mohr–Coulomb failure criterion. When the calculated shear stress $\tau$ is less than the peak stress $\tau_y$ the stress-deformation relation is linear with joint stiffness $K_s$, $K_r$.

Sliding takes place if the shear stress $\tau$ reaches the peak stress $\tau_y$ and stress drop occurs. The shear stress becomes equivalent to residual strength $\tau_r$ and stress drop $\Delta\tau_d$ ($= \tau_y - \tau_r$) is released and spread to nearby elements. In this way, the released stress drop in the hypocentre is triggered and the shear failure spreads to surrounding areas with increasing shear stress.

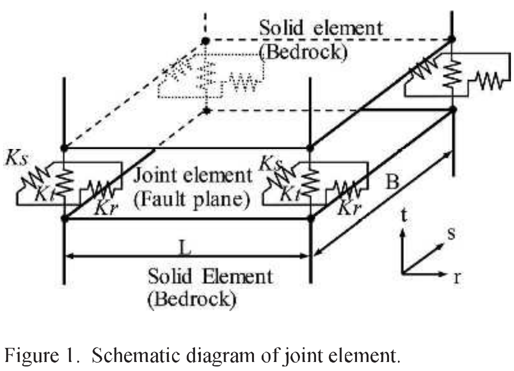


Figure 1. Schematic diagram of joint element.

### 2.3 *ΔCFF*

ΔCFF caused by main shock rupture effectively explains the aftershock distributions for earthquakes triggered by stress changes of more than 0.1 MPa. For a given fault plane and slip vector, stress change can be quantified as

$$\Delta CFF = \Delta\tau + \mu'\Delta\sigma \tag{2}$$

where $\Delta\tau$ is the shear stress change in the slip direction on the potential fault, $\Delta\sigma$ is the normal stress change (positive for compression) and $\mu'$ is the effective friction coefficient that is often used with the assumed value, e.g. 0.4 (King et al. 1994, Stein et al. 1997). If ΔCFF > 0, slip potential is enhanced; if ΔCFF < 0, it is inhibited. ΔCFF for 3D-FEM is calculated from stress change at the end of fault rupture.

## 3 ANALYTICAL CONDITIONS AND PARAMETERS

### 3.1 *Fault parameters*

The bedrock is a uniform isotropic medium with an elastic velocity of $Vp = 6.1$ km/s and $Vs = 3.5$ km/s. The fault plane is 15 km in length and 10 km in depth from surface ground and hypocentre is located at 5km depth. We examined two fault types: (i) a strike slip fault with left-lateral slip and (ii) a trust fault. The strike slip fault plane dips at 90° with a rake angle of $\lambda = 180°$. The trust fault plane dips at 50° and we assumed two rake angle cases: $\lambda = 90°$ (trust fault) and $\lambda = 120°$ (trust fault with left-lateral slip). Table 1 presents the parameters for the strike slip fault, which were calculated from the fault area based on Recipe for predicting strong motion (Irikura 2006). To compare the influence of fault type, the parameters used for the trust fault were the same as those for the strike slip fault.

### 3.2 *Stress conditions for 3D-FEM*

It is necessary to set fault plane strength and initial stress distribution because the amount of dislocation on the fault plane is not an input parameter. To compare the influence of the shape of the initial stress distribution, we examined two stress distribution types, as shown in Figure 2: the mountain type and asperity type. Shear stress in the asperity type was con-

Table 1. Parameters for strike slip fault.

| | |
|---|---|
| Fault length, $L$ × width, $W$ | 15 km × 10 km |
| Asperity length, $L_a$ × width, $W_a$ | 1.8 km × 1.8 km |
| Seismic moment, $M_0$ | $1.74 \times 10^{18}$ N·m |
| Dip angle, $\delta$ | 90° |
| Average stress drop, $\Delta\tau_s$ | 2.3 MPa |
| Stress drop in asperity, $\Delta\tau_a$ | 15.6 MPa |
| Slippage in asperity, $D_a$ | 70.3 cm |
| Slippage in back ground, $D_b$ | 29.0 cm |

centrated only at the hypocenter. Residual strength $\tau_r$ makes 10.0 MPa sufficiently larger than dynamic stress drop $\Delta\tau_d$ and peak strength is set by adding stress drop in asperity in Table 1 to residual strength. Excess strength $\Delta\tau_e$ in the mountain type was 1.6 times the static stress drop $\Delta\tau_s$ (Andrew 1976), and $\Delta\tau_d$ was 6.0 MPa, as shown in Figure 2. The shape of the peak stress distribution is a square, and the area of peak strength is calculated so that the volume of the truncated square pyramid shown as a blue solid line is equal to the volume of the cube shown as a dashed line. The shear stress at the hypocentre is assumed to be slightly larger than the peak strength $\tau_y$.

Seismic response in the 3D-FEM is dependent on shear stiffness $ks$ of the joint element (Iwata et al. 2018); therefore, we compared ΔCFF for the case of $ks = 1.0$ GN/m$^3$ with that of $ks = 1.0 \times 10^4$ kN/m$^3$.

### 3.3 *FEM model*

Figure 3 shows the 3D-FEM model for the strike slip fault. Joint elements are set up from the left-lateral boundary to the right lateral boundary and the strength of joint elements located inside or outside of the fault plane have sufficient strength not to fail. The distance from the fault edge to the boundaries is greater than the fault length and viscous dampers were introduced at the lateral and bottom boundaries to absorb scattering wave energy. When acceleration response is estimated using FEM, it is necessary to change the mesh height according to the natural frequency of object facilities, however, displacement and stress response do not depend on the mesh height (Iwata et al. 2018). In this study, the mesh height

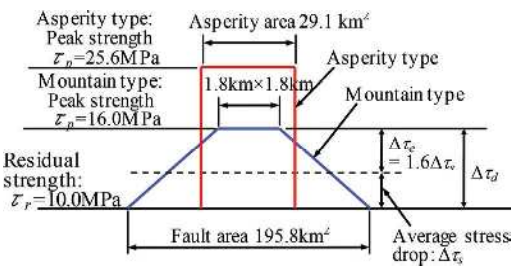


Figure 2. Schematic diagram of initial stress distribution.

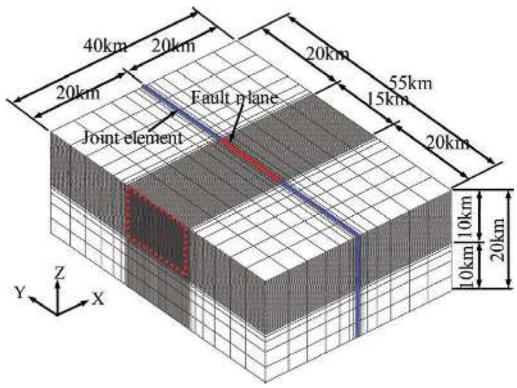


Figure 3. 3D-FEM mesh for strike slip fault.

around the fault plane was 250 m in order to express the changes in slippage and stress distribution.

## 4 ANALYSIS RESULTS BASED ON ELASTICITY THEORY OF DISLOCATION

Figure 4 shows the ΔCFF distribution at 5 km depth corresponding to the earthquake focal depth for the strike slip fault. The fault plane slipped in the direction indicated by white arrows in Figure 4. The positive domain spread radially towards the outside from the fault edge. The negative domain appeared on both sides of fault plane. The positive domain spreading from the asperity edge occurred because of extreme difference between the slip amount of the asperity area and that of background area.

Figure 5 shows the ΔCFF distribution at 5 km depth for the trust fault. The positive domain spreads from the fault edge and through the frontal domain, as illustrated by the white arrow. The domain of ΔCFF > 0.1 MPa where seismicity is enhanced becomes smaller than that of the strike slip fault.

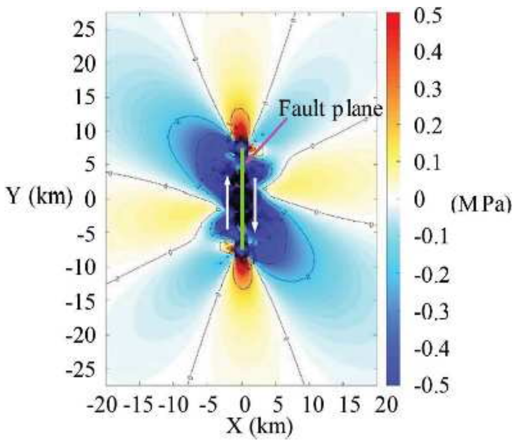


Figure 4. ΔCFF distribution at 5 km depth for strike slip fault.

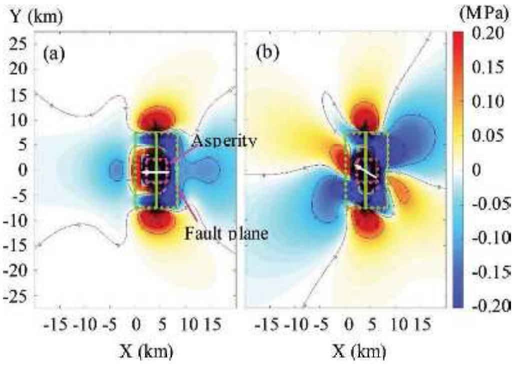


Figure 5. ΔCFF distribution at 5 km depth for the trust fault: (a) $\lambda = 90°$, (b) $\lambda = 120°$ (trust fault with left-lateral slip).

## 5 ANALYSIS RESULTS BASED ON 3D-FEM

### 5.1 *Influence of initial stress distribution*

We carried out fault rupture simulations using different initial stress distributions: mountain type and asperity type, and compared slip distributions on the fault plane and ΔCFF distributions at 5 km depth. The fault type was strike slip and the spring stiffness of the joint element was 1 $GN/m^3$. Figure 6 shows the slip distributions and Figure 7 shows the ΔCFF distributions. The maximum slip amount for the mountain type was 1.26 m and the rupture front reached the ground surface. The maximum slip amount for the asperity type was 2.08 m, i.e. larger than that of the mountain type, although the rupture front did not reach the ground surface. The positive domain along the extending direction of the fault plane in the mountain type occurred from the fault edge, whereas that of the asperity type occurred from halfway across the fault plane because sliding stopped in the middle of the fault plane. The ΔCFF > 0.1 MPa domain in the mountain type spread farther than it did for the asperity type. The positive domain and quantity of ΔCFF on both sides of the fault plane in the asperity type were larger than that of the mountain type because of the larger amount of slip.

### 5.2 *Influence of spring stiffness of the joint element*

We conducted fault rupture simulations for the strike slip fault using different spring constants: $ks = 1.0$ and 0.01 $GN/m^3$. The fault type was strike slip and the initial stress distribution was mountain type. Figures 8 and 9, respectively, show the slip and ΔCFF distributions for $ks = 0.01$ $GN/m^3$. The slipping area and maximum slip amount for $ks = 0.01$ $GN/m^3$ were smaller than those of $ks = 1.0$ $GN/m^3$, as shown in Figures 6(b) and 7(b). If shear failure occurs in a joint element, stress drop occurs and the released stress spreads to nearby elements. When a shear spring constant is set to a smaller value, the shear stress of the fault transferred from a yield element becomes smaller, as does fault sliding; ΔCFF also becomes smaller for those reasons.

### 5.3 *Influence of fault type*

We performed fault rupture simulations for different fault types: a strike slip fault and a trust fault with $\lambda$=90° and 120°. The initial stress distribution was mountain type and the spring stiffness of the joint element was 1 $GN/m^3$. Figure 10 shows the slip distribution for the trust fault with $\lambda$=90°. The maximum slip amount in the mountain type was 1.74 m and the rupture front reached the ground surface.

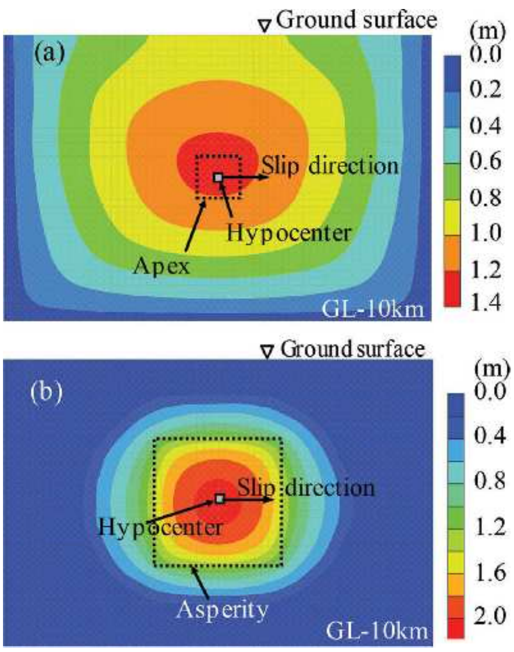


Figure 6. Comparison of slip distributions in different initial stress distributions for strike slip fault: (a) mountain type, (b) asperity type.

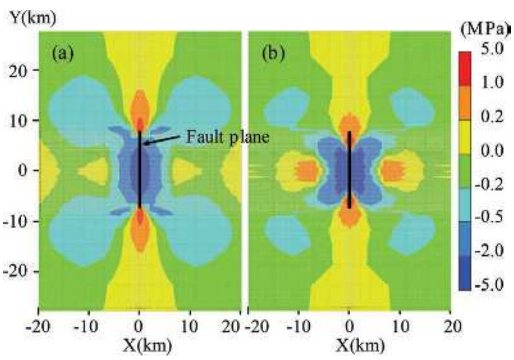


Figure 7. Comparison of ΔCFF distribution at 5 km depth for different initial stress distributions of the stroke slip fault: (a) mountain type, (b) asperity type.

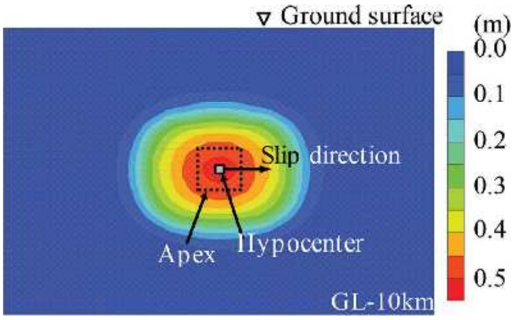


Figure 8. Slip distributions using joint spring constant of $ks$ = 0.01 GN/m$^3$ for strike slip fault.

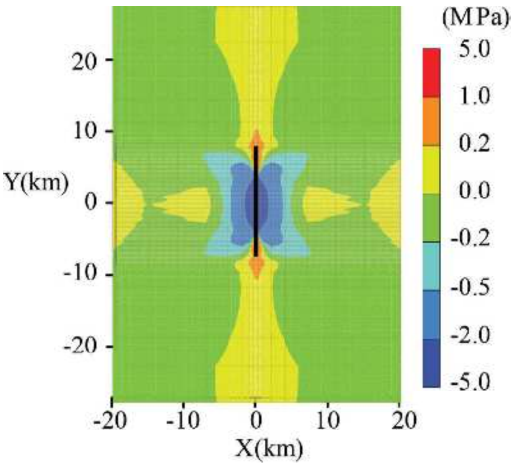


Figure 9. ΔCFF distribution at 5 km depth using joint spring constant of $ks$ = 0.01 GN/m$^3$ for strike slip fault.

When the rake angle was 120°, the rupture front spread upwards diagonally and the maximum slip amount became 1.65m; i.e. smaller than for λ=90°.

Figure 11 shows the comparison of ΔCFF distributions at 5 km depth. In case of λ=90°, the ΔCFF > 0.2 MPa domain shown in orange in Figure 11(a) distributes radially at both edges of the fault plane.

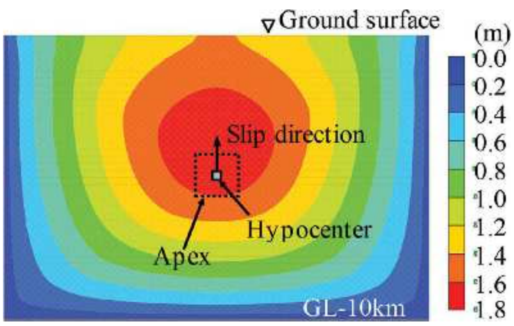


Figure 10. Slip distributions for trust slip fault (λ = 90°).

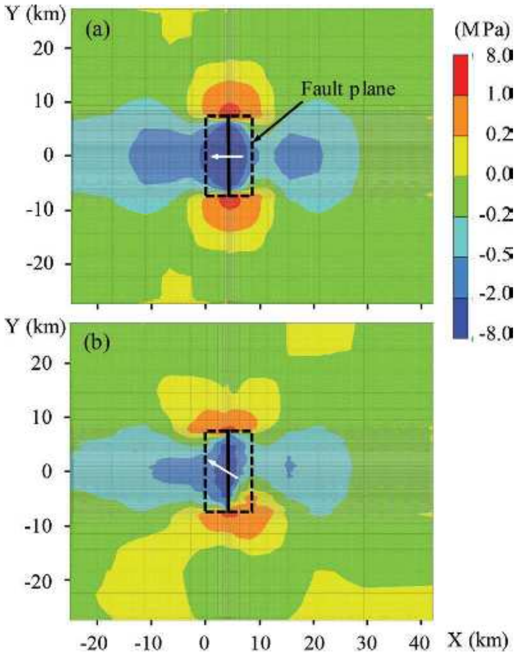


Figure 11. Comparison of ΔCFF distribution at 5km depth in different rake angles for trust fault: (a) λ = 90°, (b) λ = 120°.

A positive domain before and after the sliding direction seen in the strike slip fault did not occur because the rupture front reached the ground surface and the shear stress was released. The positive and negative domain for λ=120° extended to the sliding direction and the area became smaller than that of λ=90°.

## 6 COMPARISON OF ANALYTICAL METHODS

In this study, we estimated fault parameters based on Recipe. The slip amount calculated by 3D-FEM was larger than that of Recipe and ΔCFF based on 3D-FEM was larger than that of the elasticity theory of dislocation.

The shape of sliding distribution on the fault plane by 3D-FEM varied according to analysis conditions; nevertheless, in all cases, the amount of sliding changed smoothly. Unlike the assumption in Recipe, sliding did not concentrate only on asperity. For the elasticity theory of dislocation, shear stress was concentrated around the outer circumferential portion of asperity where the difference in slippage was large and ΔCFF became large. However such a concentration was not seen for 3D-FEM, and the shape of the ΔCFF distribution based on 3D-FEM differed from the discrepancy in the elasticity theory on both sides of the fault plane.

When rupture simulation was conducted using the initial stress distribution of the mountain type and a joint stiffness of $ks$ = 1.0 GN/m$^3$, the maximum slip amount was more than 1.2 m and seismic moment calculated from the slip distribution was estimated to be greater than $3.0 \times 10^{18}$ N·m. These values are considerably larger than those assumed by Recipe. When we used the initial stress distribution of the asperity type, the maximum slip amount increased to 2.08 m but the estimated seismic moment was smaller than $3.0 \times 10^{18}$ N·m because the sliding area was smaller.

On the other hand, with a joint stiffness of $ks$ = 0.01 GN/m$^3$ and the initial stress distribution of the mountain type, the maximum slip amount became 0.52 m and seismic moment was estimated as 1.43 $\times 10^{18}$ N·m. These results are slightly smaller than those assumed by Recipe.

As a result, when the initial stress distribution was of the asperity type and the joint stiffness $ks$ was set to around 0.01 GN/m$^3$, the calculated slippage and seismic moment values were closer to those of Recipe. In previous studies on the 2014 Northern Nagano Earthquake, for which the shear spring constant was $K_s$ = 0.01 GN/m$^3$, the rupture did not propagate and only the immediate vicinity of the hypocentre was ruptured (Iwata et al. 2018). Moreover, the surface displacement when using initial stress distribution of the asperity type was markedly larger than that of the observations. A challenging future problem will be to examine what combination of parameters best reproduces the observations.

## 7 CONCLUSIONS

In this study, we calculated static ΔCFF for simple fault rupture models using the elasticity theory of dislocation and 3D-FEM. We compared the distribution shape and quantity of ΔCFF. The findings obtained from this study can be summarised as follows:

1. The slippage and seismic moment calculated by 3D-FEM using fault parameters based on Recipe become considerably larger than those assumed by Recipe (except for a joint stiffness of $ks$ = 0.01 GN/m$^3$).
2. The distribution shape of ΔCFF in 3D-FEM is similar to that given by the elasticity theory of dislocation outside of the fault edge, but it is markedly different around the asperity owing to the difference in displace distribution.
3. The sliding domain in the initial stress distribution of the asperity type is smaller than that of the mountain type, but the amount of slide is larger. Therefore, the distribution range of the asperity type becomes smaller and the value of ΔCFF around the fault plane becomes larger.
4. The slip amount and ΔCFF become smaller as the joint stiffness is set smaller.
5. Regarding trust faults, the positive domain of ΔCFF distributes radially at both edges of the fault plane and extends towards the sliding direction.

Even if fault type and seismic magnitude such as fault geometry and moment magnitude are the same, the distribution domain and quantity of ΔCFF differ greatly according to the combination of analytical parameters. Therefore, it is necessary to examine the methods used for setting parameters in the model to reproduce actual fault movements. We continue to examine the validity and applicability of fault rupture simulations using 3D-FEM to evaluate rupture propagation and fault activity.

## REFERENCES

Andrew, D.J. 1976. Rupture velocity of plane strain shear racks, *J. of Geo. Res.*, Vol. 81, No. 32, 5679–5687.

Gomberg, J., Bodin, P. & Reasenberg, P. A. 2003. Observing earthquakes triggering near-field by dynamic deformations, *Bull. Seis. Soc. Am.*, 93: 118–138.

Hashimoto, M. 1996. Static stress changes associated with the Kobe earthquake: Calculation of changes in Coulomb failure function and comparison with seismicity change. *J. Seismol. Soc. Jpn.*, 48: 521–530.

Irikura, K. 2006. Predicting strong ground motions with "Recipe", *Bull. Earthq. Res. Inst. Univ. Tokyo*, 81: 341–352.

Iwata, N., Kiyota, R., Adachi, K., Takahashi, Y., Aydan, Ö., Miura, F. & Ito, T. 2018. Simulation of strong motions and surface rupture of the 2014 Northern Nagano Earthquake. *Proc. of the 3rd inter. conf. on Rock dynamics and applications (ROCDYN-3), Norway*: 541–546.

Iwata, N., Kiyota, R., Aydan, Ö., Ito, T. & Miura, F. 2019. Effects of Fault geometry and subsurface structure model in strong motion and surface rupture induced by the 2014 Kamishiro Fault Nagano Earthquake. *Proc. of 2019 Rock Dynamic Summit in Okinawa (2019RDS)* (under submission).

Kilb, D., Gomberg, J. & Bodin, P. 2002. Aftershock triggering by dynamic stresses, *J. Geophys. Res.* 107(B4): 2060, doi:10.1029/2001JB000202.

King, G. C. P., Stein, R. S. & Lin, J. 1994. Static stress changes and the triggering of earthquakes, Bull. Seis. Soc. Am., 84: 935-953.

Mizumoto, T., Tsuboi, T. & Miura, F. 2005. Foundamental study on failure rupture process and earthquake motions and near a fault by 3D-FEM. *Journal of Japan Society of Civil Engineers* 780/I-70: 27–40 (in Japanese with English abstract).

Okada, Y. 1992. Internal deformation due to shear and tensile faults in a half-space. Bull. Seismol. Soc. Am. 82: 1018–1040.

Stein, R. S., Barka, A. A., & Dieterich, J. H. 1997. Progressive failure on the North Anatolian fault since 1939 by earthquake stress triggering. *Geophys. J. Int.* 128: 594–604.

Toda, S., Stein, R.S., Reasenberg, P.A., Dieterich, J.H. & Yoshida, A. 1998. Stress transferred by the 1995 Mw = 6.9 Kobe, Japan, shock: Effect on aftershocks and future earthquake probabilities. *J. Geophys. Res.* 103: 24543–24565.

Toda, S., Stein, R.S., Sevilgen, V. & Lin, J. 2011. Coulomb 3.3 graphic-rich deformation and stress-change software for earthquake, tectonic, and Volcano Research and Teaching—user guide. *USGS Open-File Report* 2011–1060.

Toki, K. & Sawada, S. 1988. Simulation of the fault rupture process and near filed ground motion by the three-dimensional finite element method. *Proc. of 9th World Conf. on Earth. Eng., Japan*, Vol. II: 751–756.

Tsuboi, T. & Miura, F. 1996. Simulation of stick-slip shear failure of rock masses by a nonlinear finite element method. *Journal of Japan Society of Civil Engineers* 537/I-35: 61–76 (in Japanese with English abstract).